Optics Letters

LSTM-assisted OFDR for DMGD characterization of a short few-mode fiber

GUANGKUI TAO, SIHAN QI, QINGBO LIU, XIUYUAN SUN, ZHONGYANG XU,* AND SHILONG PAN

National Key Laboratory of Microwave Photonics, Nanjing University of Aeronautics and Astronautics, Nanjing 210016, China
*xzy@nuaa.edu.cn

Received 30 April 2026; revised 6 June 2026; accepted 15 June 2026; posted 16 June 2026; published 30 June 2026

We demonstrate an LSTM-assisted optical frequency domain reflectometry (OFDR) method for differential modal group delay (DMGD) characterization of short few-mode fibers. Sparse phase-domain resampling is first applied to compensate for laser sweep nonlinearity with a low sampling rate. Then, the resampled beat signal is extrapolated by an LSTM network to improve the resolution. In a 5-m single-mode fiber, the distance resolution is improved from 4.95 mm to 0.44 mm with a 20.74-GHz sweep bandwidth. The method resolves the overlapped LP_{01} and LP_{11} modal peaks in 1-m and 6-m two-mode fibers, yielding a differential modal group delay of 1.911 ps/m for the 1-m fiber, in good agreement with the reference values. A 2.2-m four-mode fiber is further tested to demonstrate the applicability of the method. It provides a route for modal characterization of short fibers under a limited sweep bandwidth.

https://doi.org/10.1364/OL.604014

Differential modal group delay (DMGD) is a key parameter in mode-division multiplexing systems, which characterizes the group-velocity difference between modes. Optical frequency domain reflectometry (OFDR) is an effective approach for DMGD characterization, which has been widely used for high-precision fiber characterization [1–3]. In OFDR, the beat signal between the reference and the backscattered signal is transformed via the Fourier transformation to obtain the spatial response along the fiber [4]. Since the achievable spatial resolution is mainly determined by the sweep bandwidth of the tunable laser [5], resolving closely spaced reflection points generally requires a large optical sweep bandwidth [6,7]. Conventional DMGD measurements usually require hundreds of meters of fibers to accumulate sufficient modal delay, making them unsuitable for meter-scale fibers [8,9]. Hence, it is still challenging to obtain the modal delay difference in short few-mode fibers (FMFs) with limited bandwidth [10].

In recent years, several methods have been proposed to enhance OFDR resolution by broadening the sweep bandwidth [11–13]. However, these approaches usually increase system complexity and cost, and may aggravate sweep nonlinearity [14]. Resampling and deskew filtering can compensate sweep nonlinearity [15–17], but they do not overcome the resolution limit imposed by the available sweep bandwidth. Machine-learning-based signal processing has recently shown potential for optical sensing and frequency-modulated continuous-wave (FMCW) ranging enhancement [18–20], suggesting a possible route to enhance the resolution of a bandwidth-limited OFDR.

Several signal-processing algorithms have been used for resolution enhancement in the band-limited sensing systems. Autoregressive (AR) spectral extrapolation estimates missing frequency components from the available high signal-to-noise-ratio (SNR) band, which has been applied to enhance the reflective depth-resolution [21]. Burg-based AR spectral estimation has been used in OFDR to reduce spectral broadening [22]. Matrix Pencil provides a high-resolution parametric estimator by modeling the beat signal as a sum of complex exponentials beyond the FFT-bin limitation [23]. Temporal convolutional networks (TCNs) have also been used for time-series forecasting by extracting long-term temporal patterns with dilated causal convolutions [24]. However, their ability to preserve closely spaced modal spectral structures in short FMFs remains to be evaluated.

In this work, we propose an OFDR method combining sparse phase-domain resampling (SPDR) and long short-term memory (LSTM)-based signal extrapolation for short-fiber DMGD characterization. SPDR compensates sweep nonlinearity with a low sampling rate, and the LSTM network extends the beat-signal sequences to improve resolution. The method is validated using a 5-m single-mode fiber (SMF), 1-m and 6-m two-mode fibers (TMFs), and a 2.2-m four-mode fiber. Quantitative comparison with AR, TCN, and Matrix Pencil methods further verifies the advantage of LSTM in preserving the modal spectral structure for DMGD extraction.

The experimental setup is shown in Fig. 1. A tunable laser source (TLS) centered at 1550 nm is linearly swept. The optical output is divided into a main interferometer and an auxiliary interferometer. The auxiliary interferometer is used for phase resampling, in which the path difference is 27 m, corresponding to a delay of 131.4 ns. The beat frequency in the auxiliary interferometer is 3.28 MHz. For a linearly swept signal $\nu(t) = \nu_0 + \gamma t$, the frequency-swept bandwidth $B = \gamma T$, where T is the period of a chirp. The conventional OFDR spatial resolution is:

$$\Delta z_0 = \frac{c}{2 n_g \gamma T}, \tag{1}$$

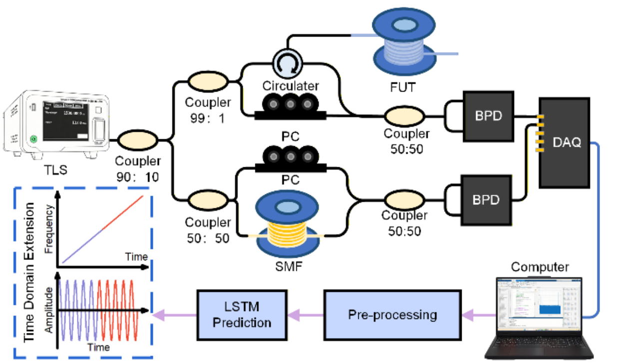

Fig. 1. OFDR system and signal-processing flow. BPD, balanced photodetector; DAQ, data acquisition card; FUT, fiber under test; PC, polarization controller; SMF, single-mode fiber; TLS, tunable laser source.

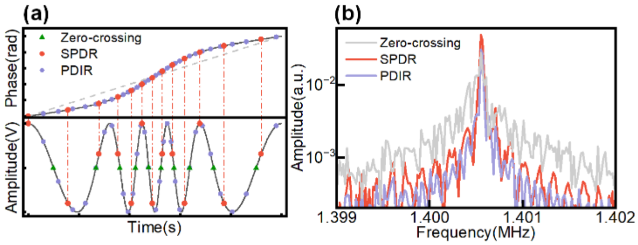

Fig. 2. Comparison of three resampling strategies. (a) Schematic illustration of zero-crossing resampling, SPDR, and PDIR. (b) Spectra obtained by the three methods. For the comparison in (b), the phase intervals of PDIR and SPDR are 0.3π and 1.5π, respectively.

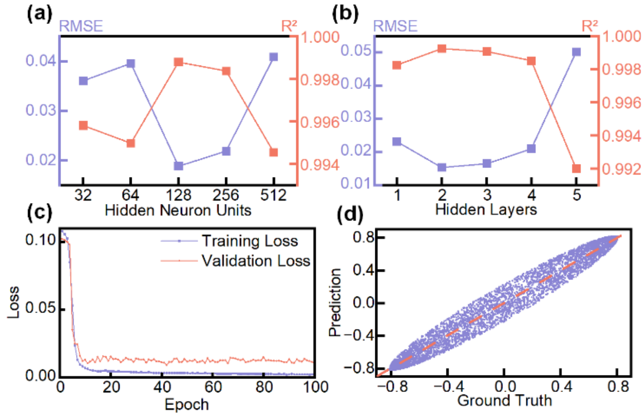

Fig. 3. LSTM model selection and validation. (a) Validation RMSE and R^2 versus hidden units. (b) Validation RMSE and R^2 versus hidden layers. (c) Training and validation losses. (d) Predicted versus ground-truth values on the test set.

where n_g is the group refractive index.

Due to the nonlinear frequency sweeping, the direct FFT of the raw beat signal broadens the spectral peaks. SPDR is applied to suppress this effect. The instantaneous phase $\phi_a(t)$ of the auxiliary interference signal $I_a(t)$ is obtained by a Hilbert transform. After phase unwrapping, a uniform phase grid is obtained as $\phi_k = \phi_0 + k\Delta\phi$, where ϕ_0 is the initial phase, $\Delta\phi$ is the phase increment, and k is an integer. Then, the main interferometer signal is resampled as $s_r[k] = s(t_k)$, where t_k is the time corresponding to ϕ_k. Figure 2(a) illustrates the principle of zero-crossing resampling, conventional phase-domain interpolation resampling (PDIR), and SPDR. Zero-crossing resampling samples at the zero crossings of the auxiliary signal, whereas PDIR and SPDR both use uniform phase-domain grids.

Unlike PDIR, conventional phase-domain interpolation resampling (PDIR), which uses a small phase increment for dense interpolation, SPDR uses a larger phase increment to reduce the effective sampling rate while preserving the details of beat signals. The effective sampling rate after SPDR can be approximately expressed as:

$$f_s^{\mathrm{SPDR}} \approx \frac{2\pi f_a}{\Delta\phi}, \tag{2}$$

where f_a is the beat frequency of the auxiliary interferometer. To avoid aliasing, $\Delta\phi$ is selected according to the highest beat frequency of interest $f_{b,\max}$ in the main interferometer signal, satisfying $f_s^{\mathrm{SPDR}} \geq 2f_{b,\max}$. As shown in Fig. 2(b), SPDR provides a spectral response close to that of PDIR with a much sparser sampling grid, and both methods yield narrower spectral peaks than zero-crossing resampling.

After SPDR, the signal is bandpass filtered and normalized before being fed into the prediction network. Two input channels are used, namely the instantaneous amplitude and the instantaneous phase increment. To reduce long-term phase drift, the loss function includes phase-increment error, accumulated phase error, and mean phase-increment bias terms. For each measurement condition, multiple beat-signal records are acquired to generate 3500 samples using a sliding-window scheme. These samples are divided into training, validation, and test sets with a ratio of 60:20:20. For performance evaluation, reference signals are independently acquired with a larger sweep bandwidth and are used only as experimental baselines rather than network inputs or training labels. The LSTM architecture and training strategy remain unchanged, while the training dataset is selected for each measurement condition.

A two-layer LSTM network was used to extrapolate the beat signals, with 128 hidden units per layer and a dropout rate of 0.2. The network was trained using the mean-square-error loss and the Adam optimizer, with a learning rate of 0.001 and a batch size of 64. The final architecture was selected according to the validation root-mean-square error (RMSE) and R^2. The training time was approximately 20 min on RTX 4090, and the inference time for a single measurement was approximately 26.8 ms. Figure 3 shows the model selection and validation results. The validation RMSE and R^2 identify the 128-unit and two-layer configuration as the best model. The loss curves converge without obvious overfitting, and the test-set predictions are close to the ground-truth values.

The trained LSTM network was then used to extrapolate the beat signal and enhance the effective resolution. Here, the LSTM network is not used as a feedforward mapping from the input signal to a sharpened spectrum. It extends the SPDR processed beat signal in the time domain, and the resolution improvement is obtained from Fourier analysis of the longer effective signal. The beat signal is extrapolated from the measured duration T_0 to $T_{eff} = T_0 + T_p$, where T_p denotes the predicted duration. The effective analyzed span B_{eff} is therefore:

$$B_{eff} = \gamma\left(T_0 + T_p\right), \tag{3}$$

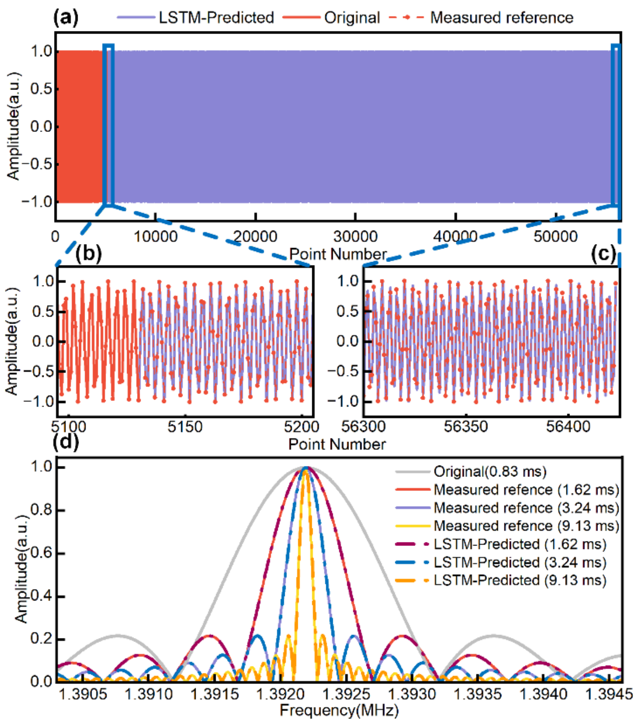

Fig. 4. LSTM-based extrapolation for a 5-m SMF. (a) Original input, LSTM-predicted signal, and reference signal. (b) Enlarged view of the input-prediction junction. (c) Enlarged view near the end of the extrapolated record. (d) Normalized spectra for different effective durations.

and the corresponding effective distance resolution Δz_{eff} is:

$$\Delta z_{eff} = \frac{c}{2n_g\gamma\left(T_0 + T_p\right)}. \tag{4}$$

A 5-m SMF was first used to validate the prediction accuracy and resolution enhancement. After SPDR, the effective resampling rate was 6.18 MS/s. A 5130-point input sequence, corresponding to 0.83 ms, was extrapolated to 9.13 ms. A reference signal with equal duration was also recorded. Figures 4(a)–4(c) compare the input, the LSTM-predicted signal, and the reference signal, showing continuous waveform transition and long-range prediction consistency.

The normalized spectra in Fig. 4(d) show that the corresponding resolution decreases from 4.95 mm to 2.54 mm, 1.27 mm, and 0.44 mm as the effective duration is extended to 1.62, 3.24, and 9.13 ms, respectively. It should be noted that the 0.44-mm nominal resolution is achieved with a 20.74-GHz bandwidth. Achieving the same resolution by conventional optical sweeping would require approximately 233.29 GHz, corresponding to 11.25 times the present bandwidth. The method was then applied to DMGD characterization of 1-m and 6-m TMFs supporting LP_{01} and LP_{11} modes. Because closely spaced modal peaks produce both slow envelope modulation and fast carrier oscillation, the TMF model used a 256-step input window and a 16-step prediction length for recursive extrapolation.

For the 1-m TMF, the effective resampling rate was 6.65 MS/s, with input and output durations of about 20 ms and 60 ms, respectively. The same LSTM settings are used for the 6-m TMF, with input and output durations of about 3 ms and 9 ms, respectively. The DMGD was calculated from the beat-frequency

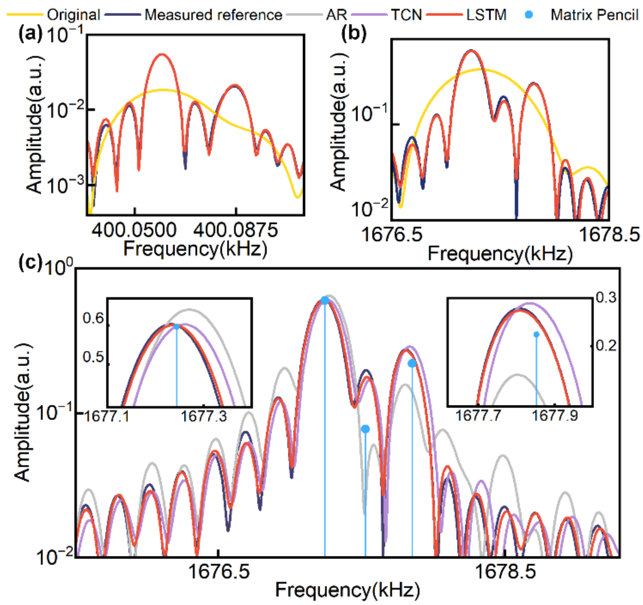

Fig. 5. DMGD characterization of TMFs. (a) Spectra of the original, LSTM-predicted signal, and reference signal for the 1-m TMF. (b) Spectra for the 6-m TMF. (c) AR, TCN, Matrix Pencil, and LSTM reconstruction results for the 6-m TMF.

spacing between the two modal peaks as:

$$\mathrm{DMGD} = \frac{\Delta f_b}{2\gamma L}, \tag{5}$$

where Δf_b is the frequency spacing between the two modal peaks, and L is the fiber length. The factor of 2 accounts for the round-trip propagation in the OFDR configuration.

Figure 5(a) shows the results of the 1-m TMF. The original measured spectrum shows strongly overlapped modal peaks, while the LSTM-predicted spectrum resolves two peaks in good agreement with the reference signal. The DMGD values extracted from the reference and predicted spectra are 1.896 and 1.911 ps/m, respectively, both close to the manufacturer-provided time-of-flight (ToF) value of 1.9 ps/m. Figure 5(b) shows the results of the 6-m TMF, where the larger accumulated modal delay gives more clearly separated peaks. The LSTM-predicted spectrum agrees well with the reference spectrum, indicating that the modal spacing required for DMGD extraction is preserved.

Figure 5(c) compares AR, TCN, Matrix Pencil, and LSTM under the same 6-m TMF condition. AR gives the poorest reconstruction, with obvious peak-position deviations, amplitude mismatch, and spectral-profile distortion. Matrix Pencil provides discrete frequency estimates rather than a fitted amplitude spectrum. Its estimated modal frequencies are closer to the reference peaks than AR, but less accurate than TCN and LSTM. TCN better reproduces the modal peaks with smaller position and amplitude deviations, whereas LSTM gives the best overall agreement with the reference in peak position, amplitude, and spectral profile.

Table 1 gives the average absolute errors of the two modal peak frequencies and the extracted DMGD with respect to the reference signal over ten repeated tests. The average DMGD obtained from the measured reference is 1.942 ps/m. For each test, the two peak-frequency errors were calculated as $|\Delta f_i| =$

Table 1. Average Absolute Peak-Frequency and DMGD Errors with Respect to the Measured Reference for the 6-m TMF

Method	$\lvert\Delta f_1\rvert$(Hz)	$\lvert\Delta f_2\rvert$(Hz)	$\lvert\Delta$DMGD$\rvert$(ps/m)
AR	10.3	40.4	0.242
TCN	7.8	9.0	0.047
Matrix Pencil	5.5	17.5	0.125
LSTM	2.0	2.3	0.015

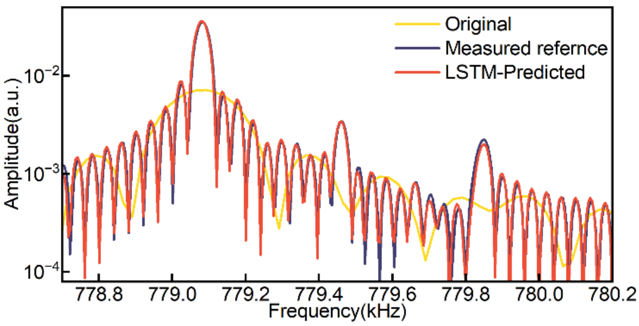

Fig. 6. Spectra of the original, LSTM-predicted, and measured-reference signals for a 2.2-m four-mode fiber.

$|f_{i,rec} - f_{i,ref}|(i = 1, 2)$ and the DMGD error was calculated as $\left|\Delta \mathrm{DMGD}_j\right| = |\mathrm{DMGD}_{j,rec} - \mathrm{DMGD}_{j,ref}|$. Table 1 lists the average absolute errors over ten repeated tests. AR gives the largest peak frequency and DMGD errors. Matrix Pencil improves the peak-frequency estimation compared with AR, but its DMGD error remains larger than that of TCN and LSTM. LSTM gives the smallest errors, indicating better preservation of the modal spectral structure.

Besides, a 2.2-m four-mode fiber was further tested, and the corresponding spectra are shown in Fig. 6. The four-mode fiber exhibits a more complicated multimode spectral response than the two-mode fiber. The closely spaced LP_{21} and LP_{02} components cannot be resolved by the present system, even after LSTM prediction. Nevertheless, the observable modal peaks can be identified. Using Eq. (5), the DMGD values extracted from the LSTM predicted spectrum are 3.424 and 6.837 ps/m, close to the measured reference values of 3.422 and 6.928 ps/m, respectively. These results demonstrate the applicability of the proposed method to short few-mode fibers beyond the two-mode case, while more closely spaced modes remain challenging.

In summary, we demonstrated an LSTM-assisted OFDR method for DMGD characterization of short few-mode fibers. SPDR compensates for laser sweep nonlinearity and reduces the sampling rate, while LSTM prediction extends the beat-signal sequences without broadband sweeping. The effective distance resolution is improved from 4.95 mm to 0.44 mm with a 20.74 GHz bandwidth, enabling DMGD extraction from 1-m and 6-m TMFs. Quantitative comparison shows that LSTM gives the smallest modal peak-position and DMGD errors among AR, TCN, Matrix Pencil, and LSTM. The 2.2-m four-mode fiber result further demonstrates the applicability of the method to short few-mode fibers with more complex multimode spectral responses.

Funding. National Natural Science Foundation of China (62171219, 62271249); Research and Practice Innovation Program of Nanjing University of Aeronautics and Astronautics (xcxjh20250405).

Disclosures. The authors declare no conflicts of interest.

Data availability. Data underlying the results presented in this paper are not publicly available at this time.

REFERENCES

1. M. E. Froggatt, D. K. Gifford, S. Kreger, *et al.*, J. Light. Technol. **24**, 4149 (2006).
2. Q. Liu, X. Fan, and Z. He, Opt. Express **23**, 25988 (2015).
3. F. Ito, X. Fan, and Y. Koshikiya, J. Light. Technol. **30**, 1015 (2012).
4. C. Liang, X. Zhou, Y. Wang, *et al.*, J. Light. Technol. **43**, 2371 (2025).
5. J. Qin, L. Zhang, W. Xie, *et al.*, Opt. Express **27**, 19359 (2019).
6. Z. Zhang, G. Yin, R. Jiang, *et al.*, J. Light. Technol. **41**, 6838 (2023).
7. S. Ohno, D. Iida, K. Toge, *et al.*, Opt. Fiber Technol. **40**, 56 (2018).
8. Z. Fu, J. Zhang, Z. Zhang, *et al.*, Opt. Lett. **46**, 2856 (2021).
9. Z. Yang, R. Mi, N. Zhao, *et al.*, IEEE Photonics J. **9**, 1 (2017).
10. X. Xu, M. Luo, J. Liu, *et al.*, Opt. Express **30**, 26341 (2022).
11. B. Wang, X. Fan, S. Wang, *et al.*, Opt. Express **25**, 3514 (2017).
12. Y. Zhu, X. Fan, Z. Zhang, *et al.*, Opt. Lett. **48**, 4937 (2023).
13. Y. Xue, X. Wang, C. Tang, *et al.*, Appl. Opt. **61**, 5435 (2022).
14. J. Yang, C. Zou, C. Lin, *et al.*, J. Light. Technol. **41**, 4035 (2023).
15. Z. Ding, X. S. Yao, T. Liu, *et al.*, Opt. Express **21**, 3826 (2013).
16. Z. Fang, C. Liang, S. Xu, *et al.*, IEEE Sens. J. **22**, 3202 (2022).
17. S. Zhao, J. Cui, and J. Tan, Sensors **19**, 3660 (2019).
18. Z. Xie, J. Tu, S. Gao, *et al.*, Opt. Laser Technol. **194**, 114434 (2026).
19. L. Huang, M. Liu, Y. Cui, *et al.*, IEEE J. Quantum Electron. **60**, 7700109 (2024).
20. C. Lin, Y. Tan, and Q. Wang, Opt. Laser Technol. **179**, 111299 (2024).
21. J. Dong, A. Locquet, and D. S. Citrin, Opt. Lett. **42**, 1828 (2017).
22. Q. Bai, Z. Shen, L. Wu, *et al.*, Opt. Lett. **49**, 2541 (2024).
23. S. Olbrich and C. Waldschmidt, in *European Radar Conference (EuRAD)* (IEEE, 2015), p. 177.
24. P. Lara-Benítez, M. Carranza-García, J. M. Luna-Romera, *et al.*, Appl. Sci. **10**, 2322 (2020).